# Combined Numerical and Experimental Study of a Slit Resonator Under Grazing Flow

Hervé Denayer* — *KU Leuven, Leuven, Belgium*
Jonathan Tournadre† — *LMS International, Leuven, Belgium*
Wim De Roeck‡, Wim Desmet§ — *KU Leuven, Leuven, Belgium*
Paula Martínez-Lera¶ — *LMS International, Leuven, Belgium*

**This study compares two numerical methods based on the Linearized Navier-Stokes equations (LNSE) for the simulation of a resonator in presence of a cold mean flow: a time domain Runge-Kutta Discontinuous Galerkin (RKDG) code and a frequency-domain high-order continuous Finite Element Method (pFEM). The results are compared to experimental data from a dedicated experimental campaign on a slit resonator. It was shown that the simulations predict the correct trends, but some discrepancies have been observed. The origin of these differences has to be investigated further. Different impedance measurement techniques are applied to the numerical and experimental data to obtain the acoustic impedance of the slit resonator. Within their respective range of validity, reasonable agreement is found between the different techniques.**



## Nomenclature

| | | | |
|---|---|---|---|
| $B$ | Width of the duct, $[m]$ | $Z$ | Acoustic impedance, $[Rayl]$ |
| $c$ | Speed of sound, $[m/s]$ | $z$ | Specific impedance, [-] |
| $f$ | Frequency, $[Hz]$ | $z_i$ | Location of microphone i, $[m]$ |
| $k$ | Acoustic wave number, $[m^{-1}]$ | $\delta$ | Flow boundary layer thickness, $[m]$ |
| $H$ | Back cavity depth, [m] | $\delta_{ij}$ | Kronecker delta function, [-] |
| $L$ | Length of the test section, $[m]$ | $\epsilon$ | Acoustic monopole source amplitude, $[Pa]$ |
| $M$ | Mach number, [-] | $\kappa$ | Thermal conductivity, $[W/(m.K)]$ |
| $p$ | Pressure, $[Pa]$ | $\lambda$ | Acoustic wavelength, $[m]$ |
| $R^{+/-}$ | Reflection coefficient of scatter matrix, [-] | $\mu$ | Dynamic viscosity, $[kg/(m.s)]$ |
| $S$ | Cross section of the channel, $[m^2]$ | $\nu$ | Kinematic viscosity, $[m^2/s]$ |
| $S_c$ | Surface of perforation, $[m^2]$ | $\tau$ | Viscous stress tensor, $[Pa]$ |
| $T$ | Absolute temperature, $[K]$ | $\Phi$ | Dissipation function, $[W/m^3]$ |
| $T^{+/-}$ | Transmission coefficient of the scatter matrix, [-] | $\rho$ | Density, $[kg/m^3]$ |
| $\mathbf{u}$ | Velocity vector, $[m/s]$ | $\omega$ | Angular frequency, $[rad/s]$ |
| $\mathbf{x}$ | Vector of the cartesian coordinate position, $[m]$ | | |

*Sub- and superscript*

| | |
|---|---|
| $\bullet_i$ | i:th component |
| $\bullet_0$ | Base flow related variables |
| $\bullet'$ | Perturbation |

*PhD. student at KU Leuven, Dept. of Mechanical Engineering, Celestijnenlaan 300B, 3001 Leuven, Belgium.
†Research Engineer at LMS International and PhD. student at KU Leuven, Dept. of Mechanical Engineering.
‡Assistant professor, Group T-Leuven Engineering College, Andreas Vesaliusstraat 13, 3000 Leuven, Belgium.
§Full Professor, Dept. of Mechanical Engineering, Celestijnenlaan 300B, 3001 Leuven, Belgium.
¶Senior RTD Engineer at LMS International, Interleuvenlaan 68, 3001 Leuven, Belgium.

*Abbreviations*

| | |
|---|---|
| BC | Boundary Condition |
| DOF | Degree of Freedom |
| LEE | Linearized Euler equations |
| LNSE | Linearized Navier-Stokes equations |
| pFEM | High-order Finite Element Method |
| (RK)DG | Runge-Kutta Discontinuous Galerkin method |

# I. Introduction

Liner materials, typically consisting of an array of Helmholtz resonators, are encountered in many applications to attenuate the tonal noise. The design of such resonator array is typically done with semi-analytical or empirical models. However, it is well known that the presence of a grazing flow over the facing sheet has an important influence on the acoustic behavior of a resonator. Resonators under grazing flow have been the subject of many experimental and numerical studies before. Different authors[1–8] have studied two- and three-dimensional resonators under grazing flow using scale-resolving simulations such as Direct Numerical Simulation (DNS) and many experimental studies on Helmholtz resonators can be found in the literature.[9–16]

It is shown that a Helmholtz resonator typically has a linear regime at low and moderate sound pressure levels ($< 130$dB). For this regime, it is expected that linearized governing equations can be used to model the acoustic behavior. This approach has been applied before to different geometries in a duct[17–19] and a linear liner concept[20] . This paper is a continuation of a previous study[21] and focuses on the study of a slit resonator under grazing flow with a hybrid methodology. Two implementations of the linearized Navier-Stokes equations (LNSE) are applied: a time-domain Runge Kutta discontinuous Galerkin (RKDG) and a frequency-domain high-order continuous finite element method (pFEM). These techniques allow to capture the linear interaction effects between an acoustic and a hydrodynamic field.

A few experimental studies on slit resonators exist, but they consider a relatively large perforation[16] or acoustic waves under normal incidence[3,6] . In order to provide the necessary validation data for the numerical simulations, a dedicated experimental campaign on a slit resonator under grazing flow has been carried out within the framework of this paper.



The first section describes the governing equations and the numerical techniques used for the numerical part of this study. A validation case from the literature, the sound radiation of a monopole in a flat plate boundary layer, is presented. Section III presents the characterization techniques applied to the slit resonator, the experimental and the numerical setup. Section IV presents the results from the different numerical techniques and the comparison with the experimental data. Section V concludes this paper with an overview of the main conclusions of this study.

# II. Numerical techniques

## A. Governing equations

In the linear regime of a resonator, it can be expected that its acoustic behavior and the influence of a grazing flow can be predicted using linearized equations. Because viscosity plays an important role in the acoustic behavior of a resonator[1,2] and its interaction with the shear layer over the orifice[22,23] , the linearized Navier-Stokes equations are the logical choice of governing equations.

Since the phenomena of interest are mainly the result of the interaction between the acoustic and vortical modes of the equations, the effect of viscosity in the entropy equation is neglected. This reduces the computational time significantly, and previous works[24–26] show that the impact of this assumption is small for problems as the one considered here. Also heat transfer can be neglected. With these assumptions, the

linearized Navier-Stokes equations can be written as:

$$\frac{\partial \rho'}{\partial t} + \frac{\partial(\rho_0 u_r' + \rho' u_{0r})}{\partial x_r} = 0$$
$$\frac{\partial \rho_0 u_s'}{\partial t} + \frac{\partial \rho_0 u_s' u_{0r}}{\partial x_r} + \frac{\partial p'}{\partial x_s} + (\rho_0 u_r' + \rho' u_{0r})\frac{\partial u_{0s}}{\partial x_r} - \frac{\partial \tau_{sr}'}{\partial x_r} = 0, \qquad \tau_{sr}' = \mu\left(\frac{\partial u_s'}{\partial x_r} + \frac{\partial u_r'}{\partial x_s} - \frac{2}{3}\frac{\partial u_k'}{\partial x_k}\delta_{rs}\right)$$
$$\frac{\partial p'}{\partial t} + u_{0r}\frac{\partial p'}{\partial x_r} + u_r'\frac{\partial p_0}{\partial x_r} + \gamma p_0 \frac{\partial u_r'}{\partial x_r} + \gamma p' \frac{\partial u_{0r}}{\partial x_r} = 0$$

This set of equations can be written in a more compact way using a matrix formulation:

$$\frac{\partial \mathbf{q}}{\partial t} + \frac{\partial \mathbf{A_r q}}{\partial x_r} + \mathbf{C q} + \frac{\partial}{\partial x_r}\left(\frac{\partial \mathbf{C_{rs} q}}{\partial x_s}\right) = \mathbf{0} \tag{1}$$

with $\mathbf{q} = \{\rho', \rho_0 u_1', \rho_0 u_2', p'\}^T$. The matrices for a 2-D problem are defined as:

$$\mathbf{A_r} = \begin{bmatrix} u_{0r} & \delta_{1r} & \delta_{2r} & 0 \\ 0 & u_{0r} & 0 & \delta_{1r} \\ 0 & 0 & u_{0r} & \delta_{2r} \\ 0 & c_0^2\delta_{1r} & c_0^2\delta_{2r} & u_{0r} \end{bmatrix}, \qquad \mathbf{C} = \begin{bmatrix} 0 & 0 & 0 & 0 \\ u_{0r}\frac{\partial u_{01}}{\partial x_r} & \frac{\partial u_{01}}{\partial x_1} & \frac{\partial u_{01}}{\partial x_2} & 0 \\ u_{0r}\frac{\partial u_{02}}{\partial x_r} & \frac{\partial u_{02}}{\partial x_1} & \frac{\partial u_{02}}{\partial x_2} & 0 \\ 0 & \frac{1-\gamma}{\rho_0}\frac{\partial p_0}{\partial x_1} & \frac{1-\gamma}{\rho_0}\frac{\partial p_0}{\partial x_2} & (\gamma-1)\frac{\partial u_{0r}}{\partial x_r} \end{bmatrix},$$

$$\mathbf{C_{rs}} = \frac{\mu}{\rho_0}\begin{bmatrix} 0 & 0 & 0 & 0 \\ 0 & -\frac{4}{3}\delta_{1r}\delta_{1s} - \delta_{2r}\delta_{2s} & \frac{2}{3}\delta_{1r}\delta_{2s} - \delta_{2r}\delta_{1s} & 0 \\ 0 & \frac{2}{3}\delta_{2r}\delta_{1s} - \delta_{1r}\delta_{2s} & -\delta_{1r}\delta_{1s} - \frac{4}{3}\delta_{2r}\delta_{2s} & 0 \\ 0 & 0 & 0 & 0 \end{bmatrix}.$$



## B. Numerical approaches

### 1. *Continuous FEM for the LNSE in frequency domain*

**pFEM formulation**

The High-order Finite Element Method is based on the variational formulation of the original problem and the approximation of the field variable distributions of the continuum domain in terms of the sum of high-order shape functions[27,28].

Here, the perturbation quantities are assumed to be harmonic time dependent variables that can be written as $q'(\mathbf{x}, t) = \hat{q}(\mathbf{x})e^{j\omega t}$, where $j$ is the imaginary unit, $\hat{q}$ is a complex quantity and $\omega$ is the angular frequency. Multiplying equations (1) by a test function and integrating over a finite volume $\Omega$ (a surface in 2D), the variational formulation of the system of equations can be derived:

$$j\omega \int_\Omega \tilde{\mathbf{q}} \cdot \mathbf{q}'\, d\Omega + \int_\Omega \tilde{\mathbf{q}} \cdot \frac{\partial \mathbf{A_r q}'}{\partial x_r}\, d\Omega + \int_\Omega \tilde{\mathbf{q}} \cdot \mathbf{C q}'\, d\Omega + \int_\Omega \tilde{\mathbf{q}} \cdot \frac{\partial \mathbf{C_{rs}}\frac{\partial \mathbf{q}'}{\partial x_s}}{\partial x_r}\, d\Omega = \mathbf{0}. \tag{2}$$

Using the Gauss' theorem and reformulating equation (2) in a more practical manner for implementation, yields to the following expression:

$$j\omega \int_\Omega \tilde{\mathbf{q}} \cdot \mathbf{q}'\, d\Omega + \int_\Omega \tilde{\mathbf{q}} \cdot \mathbf{C q}'\, d\Omega - \int_\Omega \frac{\partial \tilde{\mathbf{q}}}{\partial x_r} \cdot \mathbf{A_r q}'\, d\Omega - \int_\Omega \frac{\partial \tilde{\mathbf{q}}}{\partial x_r} \cdot \mathbf{C_{rs}}\frac{\partial \mathbf{q}'}{\partial x_s}\, d\Omega =$$
$$- \int_\Gamma \tilde{\mathbf{q}} \cdot [n_r \mathbf{A_r}]\, \mathbf{q}'\, d\Gamma - \int_\Gamma \tilde{\mathbf{q}} \cdot [n_r \mathbf{C_{rs}}]\, \frac{\partial \mathbf{q}'}{\partial s}\, d\Gamma \tag{3}$$

The terms of the right-hand side in the last equation correspond to the boundary integrals and are used to define the boundary conditions of the problem. The integral term in the dark-gray frame corresponds to the boundary conditions for the linearized Euler equations (LEE). It contains the flux matrix[29] $\mathbf{F} = [n_r \mathbf{A_r}]$

with $\mathbf{A_r}$ being the flux jacobian matrices[22]. In the case of the formulation obtained for the Linearized Navier-Stokes equations, there are additional terms on the boundary one has to deal with (highlighted in light-gray).

In the presented continuous pFEM code, the shape functions that approximate the space of variables are built from the Lobatto shape functions, which have proved to be efficient for acoustic problems based on the Helmholtz equation[30]. These Lobatto shape functions form a complete basis of polynomials of the order of at most $p$ on the reference finite elements. The same shape functions are also used to approximate the space of the weighting functions for the pFEM variational formulation.

**Boundary conditions**

**Rigid walls:** Walls are assumed impermeable and acoustically rigid. One can apply wall slip boundary conditions $\mathbf{u}'.\mathbf{n} = 0$ where the acoustic boundary layer is expected to play no significant role and no-slip flow boundary condition otherwise. In this last case, the acoustic perturbation satisfies at the wall

$$\mathbf{u}'.\mathbf{n} = 0 \qquad \text{and} \qquad \mathbf{u}'.\mathbf{t} = 0, \tag{4}$$

where $\mathbf{u}'$ is the acoustic perturbation velocity and $\mathbf{n}$ and $\mathbf{t}$ are the normal and tangential vectors to the wall, respectively. This no-slip condition on the wall limits of the computational domain allows one to consider the Gauss integrals over the boundary element containing viscous terms as null[28,31]. From an implementation point of view, this has been achieved by setting all the degrees of freedom associated with the velocity components to zero in a secondary linear system of the DOFs.

**Non reflecting boundary conditions:** On the part of the boundaries where the physical domain is unbounded but the extent of the computational domain is finite, active and passive non-reflecting characteristic boundary conditions have been implemented as described in[22,32]. Passive non-reflecting BC are obtained by setting the incoming characteristics[a] to zero. An excitation of the system can be obtained by prescribing the incoming characteristics at the inlet of the computational domain.



*2. Discontinuous Galerkin LNSE in time domain*

The Runge-Kutta discontinuous Galerkin (RKDG) method for the time-domain LNSE has been used in previous studies of orifices[23] and a slit resonator[21] under grazing flow. The implementation combines a nodal discontinuous Galerkin discretization in space with an optimized Runge-Kutta time integration scheme.

For the spatial discretization, a discontinuous Galerkin scheme is applied to an unstructured triangular mesh. Because of the simple geometry of the current case, straight edges can be used for all elements. This allows the use of the quadrature-free DG method, which is computationally more efficient.

The presence of the viscous term in the LNSE requires the discretization of a second order spatial derivative. It is known that the intuitive choice of applying the DG operator twice leads to an unstable formulation. Therefore the BR-1 mixed finite element formulation, first proposed by Bassi and Rebay[33], is used. This method adds the derivatives of the velocity as separate variables to the system of equations. In a first step, these derivatives are computed using a DG method. The LNSE equations are solved in a second step, using the velocity derivatives calculated in the first step in the expression for the viscous term. In vector form, the system of equations (1) can be written as:

$$\mathbf{w}^s - \frac{\partial \mathbf{q}}{\partial x_s} = \mathbf{0} \tag{5}$$

$$\frac{\partial \mathbf{q}}{\partial t} + \frac{\partial \mathbf{A}_r \mathbf{q}}{\partial x_r} + \frac{\partial \mathbf{f}_r^v}{\partial x_r} + \mathbf{C}\mathbf{q} = \mathbf{S} \tag{6}$$

with $\mathbf{q}$ the vector of unknowns, $\mathbf{w}^s$ the vector with the derivatives of the velocity in the $s$-direction and $\mathbf{f}^v = \mathbf{f}^v\left(\mathbf{w}^1, \mathbf{w}^2\right)$ the viscous flux vector.

The BR-1 formulation is known to be unstable when the convective term is negligible with respect to the diffusive term. For this reason, more advanced formulations with better stability properties, such as the BR-2 formulation[34,35] have been developed. However, the BR-2 formulation uses complex lift operators,

[a] corresponding to the negative eigenvalues of the method of the characteristics, as the normals of the domain are oriented toward the exterior of the domain.

which become very costly in an explicit RKDG framework and the implementation is more complex than for the BR-1 formulation. Furthermore, the stability requirements for the BR-2 formulation, through the so-called viscous CFL number, can severely restrict the timestep. Taking all this into account, the BR-1 formulation can be considered sufficient for the present purpose.

For the inter-element communication, a Lax-Friedrich flux formulation is used for the convective fluxes and a central flux for the viscous fluxes. Boundary conditions are imposed by specifying the fluxes at the boundary faces. The time integration is done using a 8 stage $4^{\text{th}}$-order Runge-Kutta scheme, optimized for the spatial discontinuous Galerkin operator. More details on the implementation can be found in reference[22] .

### C. Validation case: sound radiation in a flat plate boundary layer

In order to validate the codes for problems with a non-uniform mean flow, the propagation of the sound radiated by a monopole in a boundary layer has been computed. For this purpose, the case of a mean flow boundary layer over a plate has been selected, with the mean flow given by a Polhausen velocity profile[36,37] . Simulation results have been compared to DNS reference results, analytical and numerical simulations performed with other physical models and different numerical schemes[38,39] .

The parameters of the simulation considered here correspond to case D of reference[37] , with Mach number $M = 0.3$, and an acoustic wavelength to boundary layer thickness ratio equal to $\lambda/\delta = 1$. A monopole source has been added in the center of the computational domain, in the vicinity of the plate. Passive non-reflecting characteristic boundary conditions (setting the incoming characteristics to zero) have been imposed where the computational domain has been truncated. In the frequency domain pFEM simulation, the monopole source is obtained by adding a term in the right hand side of formulation (3):

$$S_{source} = \left\{ \frac{\epsilon}{c_0^2}, 0, 0, \epsilon \right\}^T , \tag{7}$$

where $\epsilon$ is the amplitude of the monopole source (arbitrarily chosen). Defining the source as a continuous distribution over an element (and integrating it with Gaussian quadrature) seems to lead to a better representation of the acoustic source than the implementation through a single Dirac delta function[b]. Therefore this strategy is applied in the presented work. For the RKDG method, this validation case has been presented before[22] , modelling the monopole by a harmonic source term with a Gaussian shape in space.



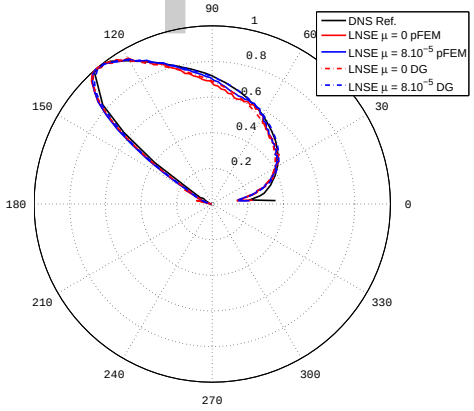


**Figure 1. Pressure directivity plot for the case of a monopole in boundary layer: normalized pressure for the reference, LEE and LNSE solutions.**

Figure 1 shows that both numerical tools give a good prediction of the pressure field in presence of the non-uniform mean flow profile. Taking the viscous effects into account yields results that correlate slightly better with the reference results for both continuous FEM and RKDG simulations. Nevertheless, the difference is small[22] and might be within the error margin of the numerical approaches. Some small amplitude oscillations can be observed in the solution for the pFEM simulation, which may stem from convergence not being fully reached. However, as the same behavior has been observed for the simulation without viscosity for the

[b] as studied in case of monopole/dipole radiation in free field

same problem, the cause is thought to be the current representation of point monopole source implemented in the pFEM code. Indeed, the numerical treatment of the dirac function at the source location, even if integrated over one element, is quite demanding for a proper representation of the acoustic source because of the dispersion error through the grid elements.

## III. Acoustic characterization of a slit resonator

### A. Impedance measurement techniques

The acoustic characterization of a Helmholtz resonator is typically done by determining its acoustic impedance, defined in frequency domain as the ratio of the acoustic pressure and the acoustic normal velocity at the wall: $Z = p/(\mathbf{u} \cdot \mathbf{n})$. Typically the impedance is normalized by the characteristic impedance of air $Z_0 = \rho_0 c_0$ in order to obtain the specific impedance $z = Z/Z_0$.

Different techniques exist to measure the impedance of a resonator in the presence of a grazing flow, the most common being the in-situ measurement and impedance eduction techniques. The following sections describe in more detail the impedance measurement techniques applied to the resonator geometry in this study.

#### *1. The in-situ impedance measurement technique*

The in-situ technique[40] computes the impedance directly from the acoustic pressure at the bottom of the resonator cavity (B) and at the facing sheet, near the perforation (A) as shown in figure 2:

$$z = -j \frac{\hat{p}_A}{\hat{p}_B} \frac{e^{j(\phi_A - \phi_B)}}{\sin(kH)} \tag{8}$$

where $\hat{p}_\bullet$ and $\phi_\bullet$ represent, respectively, the amplitude and the phase of the pressure fluctuations at the measurement points $\bullet = A, B$. The parameter $k = \omega/c_0$ represents the acoustic wavenumber in the cavity, $H$ is the depth of the backing cavity.



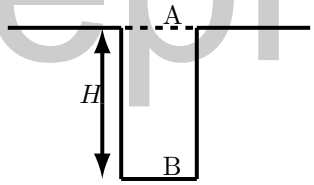


**Figure 2. Measurement setup for Dean's in-situ impedance measurement method.**

The in-situ technique makes little assumptions, only a thin facing sheet and plane wave propagation in the cavity, and provides a local value of the impedance. However, the location of the microphones is an important issue. Close to the orifice, acoustic waves are transformed into vortical and turbulent fluctuations. The hydrodynamic pressure fluctuations associated with this effect can influence the pressure signal recorded by the microphones[40,41] and compromise the accuracy of the measurement. This hydrodynamic component of the pressure also influences the results of numerical simulations[21,42] . Furthermore, the installation of the microphones in an experimental setup can be quite cumbersome.

In the present study, no experimental in-situ measurements have been done. This technique is only applied to the simulation results.

#### *2. Impedance eduction techniques*

An impedance eduction technique computes the impedance indirectly by comparing measured variables to a model for the complete test section. Therefore the accuracy of such a measurement technique is largely dependent on the accuracy of the model used. However, impedance eduction techniques don't require the cumbersome and intrusive setup of the in-situ technique. Also, the acoustic variables don't need to

be measured in the close vicinity of the resonator. It is therefore easier to suppress the influence of the hydrodynamic component of the pressure.

Different impedance eduction techniques have been developed, based on different measured acoustic quantities and models. The techniques used in this study are based on a two-port representation of the test section. A two-port element is defined as a linear acoustic system between two ducts where the plane wave propagation hypothesis is valid. This implies that the frequency is limited to the cut-off frequency of the first traversal mode in the in- and outlet duct. Such a two-port element is fully characterized by its scatter matrix, relating the left- and right-running acoustic waves at the in- and outlet of the system:

$$\begin{Bmatrix} p_2^+ \\ p_1^- \end{Bmatrix} = \begin{bmatrix} T^+ & R^- \\ R^+ & T^- \end{bmatrix} \begin{Bmatrix} p_1^+ \\ p_2^- \end{Bmatrix} \tag{9}$$

Assuming plane wave propagation in the in- and outlet duct, a minimum of two microphones in each duct is needed[43] to determine the up- and downstream propagating waves $p^+$ and $p^-$. More microphones can be used to obtain an overdetermined system, to be solved in a least-squares approach, and to suppress the effect of random errors[44]:

$$\begin{Bmatrix} p^+(f) \\ p^-(f) \end{Bmatrix} = \begin{bmatrix} e^{-jk^+z_1} & e^{jk^-z_1} \\ e^{-jk^+z_2} & e^{jk^-z_2} \\ \vdots & \vdots \\ e^{-jk^+z_n} & e^{jk^-z_n} \end{bmatrix}^{\otimes} \begin{Bmatrix} p'(z_1,f) \\ p'(z_2,f) \\ \vdots \\ p'(z_n,f) \end{Bmatrix}, \tag{10}$$

where $z_i$ represents the location of microphone $i$ with respect to the reference position at the in- or outlet of the two-port element, $k^+ \approx k/(1+M)$ and $k^- \approx k/(1-M)$ are the acoustic wave numbers of the up- and downstream propagating waves and $\otimes$ represents the Moore-Penrose pseudo matrix inverse. A further reduction of the measurement uncertainties can be obtained by using an iterative procedure to solve for certain environmental variables, as described in references[45,46].

The determination of the scatter matrix coefficients requires at least two independent measurements. These can be obtained by varying the position of the source (multiple source method) or by varying the acoustic impedance at the outlet (multiple load method). To reduce the influence of random measurement errors, more than two measurements can be used. This results in an overdetermined system, to be solved in a least-squares approach:

$$\begin{bmatrix} T^+ & R^- \\ R^+ & T^- \end{bmatrix} = \begin{bmatrix} p_{2,1}^+(f) & p_{2,2}^+(f) & \cdots & p_{2,m}^+(f) \\ p_{1,1}^-(f) & p_{1,2}^-(f) & \cdots & p_{1,m}^-(f) \end{bmatrix} \begin{bmatrix} p_{1,1}^+(f) & p_{1,2}^+(f) & \cdots & p_{1,m}^+(f) \\ p_{2,1}^-(f) & p_{2,2}^-(f) & \cdots & p_{2,m}^-(f) \end{bmatrix}^{\otimes} \tag{11}$$

By matching the obtained scatter matrix to a model for the test section, the impedance of the resonator can be determined. At low frequencies, the resonator can be considered as a lumped element and the impedance can be computed directly from the scatter matrix coefficients[13,47]:

$$\frac{Z}{\rho_0 c_0} = \frac{S_c}{S} \frac{1 - M + R_*^+/(1+M)}{1 - R_*^+ - T^+} \tag{12}$$

$$= \frac{S_c}{S} \frac{1 + M + R_*^-/(1-M)}{1 - R_*^- - T^-}, \tag{13}$$

with $R_*^\pm = R^\pm(1 \mp M)/(1 \pm M)$ and where $S$ and $S_c$ represent respectively the cross section of the channel and the surface of the perforation.

At higher frequencies the lumped impedance is no longer a good assumption and it is better to consider the impedance as distributed over the test section wall. In that case an alternative model for the scatter matrix, using the model for a rectangular duct with one lined wall[48], can be used. It was shown[c] that the method from reference[48] is equivalent to solving the following system of 5 non-linear equations:

$$\begin{cases} \frac{T^+T^- - R^+R^- + 1}{T^-} = e^{-jk_z^+L} + e^{jk_z^+L} \\ (k_x^\pm)^2 + (k_z^\pm)^2 = (k \mp M_0 k_z^\pm)^2 \\ \frac{Z}{Z_0} = j\frac{k}{k_x^\pm}\left(1 \mp M\frac{k_z^\pm}{k}\right)^2 \cot(k_x^\pm B) \end{cases} \tag{14}$$

[c] Hervé Denayer, Note on the impedance eduction technique, Internal report, KU Leuven, 2014

where $T^{\pm}$ and $R^{\pm}$ are the measured scatter matrix coefficients, $k_z^{\pm}$ and $k_x^{\pm}$ are the axial and traversal acoustic wavenumbers of the least attenuated mode in the duct of the test section, $L$ and $B$ are the length and the width of the test section and $M$ is the mean flow Mach number.

## B. Experimental setup

The experiments are carried out using the open-circuit aeroacoustic test facility of KU Leuven[49,50] , schematically shown in figure 3.

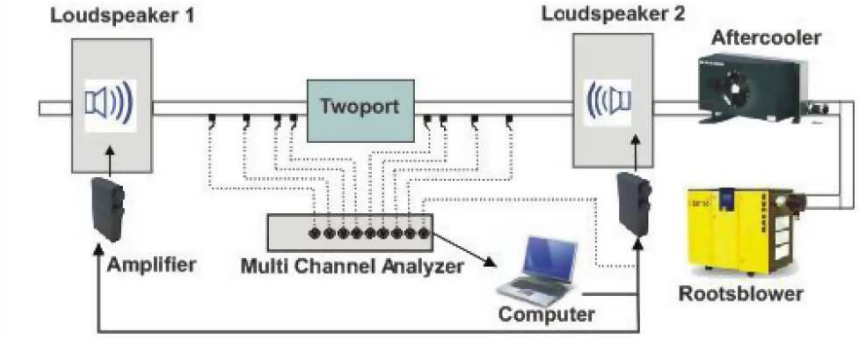


**Figure 3. Schematic overview of the experimental setup.**

A frequency regulated roots blower is used to generate a time-uniform flow in a rectangular duct (90 mm x 40 mm). For higher flow rates, a second roots blower without frequency regulator is added in parallel. For this rectangular duct, the maximum Mach number that can be achieved with the two roots blowers running in parallel, is approximately 0.25. In this study, the Mach number was limited to $M = 0.1$ in order to allow the use of linearized governing equations in the numerical part. An aftercooler is located after the roots blowers to ensure continuous and ambient temperature conditions. A vortex-flowmeter is installed afterwards to determine the mean flow rate and temperature which enters the test section. The inlet and outlet duct are equipped with 4 flush-mounted pressure transducers (type PCB 106B). At the end of each measurement section an in-line loudspeaker is installed to enable a multiple-source two-port characterization, at the downstream end various types of termination can be added to enable a multi-load approach.

Figure 4 shows the actual test section, where a slit resonator is connected to one of the long sides of the duct. The resonator consists of a rectangular cavity (50 mm x 25 mm), which is connected to the duct by a rectangular slit with a width of 1 mm. The facing sheet has a thickness of 1 mm. The cavity extends of the full width of the duct (90 mm). For manufacturing reasons, the slit ends at 2 mm from the wall at both sides of the duct.

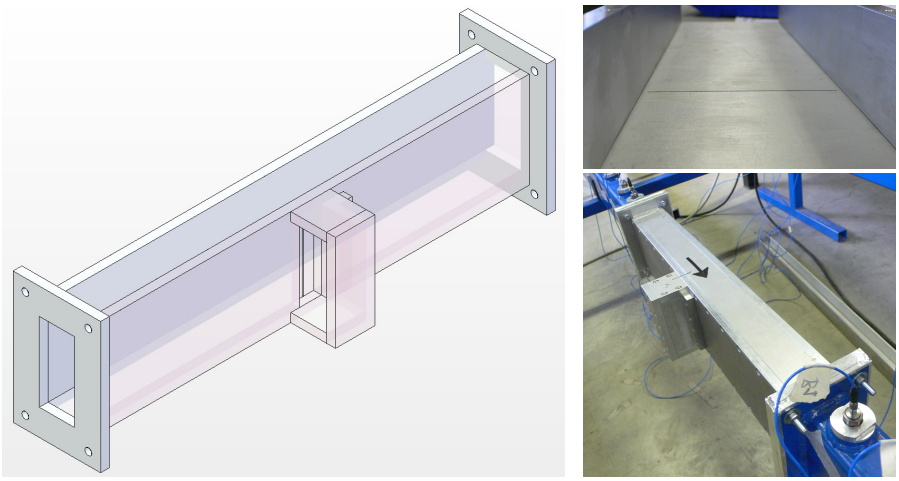

**Figure 4. Schematic overview of the test section (left) and pictures of the opened test object (top right) and the test object built into the rig (bottom right).**

A combined multiple source/multiple load approach is used with up to 4 measurements for each flow rate. The multiple source approach is achieved by using two different excitation signals, a loudspeaker at the downstream end and one at the upstream end of the duct. It has been verified that the excitation levels are sufficiently low to stay in the linear regime of the resonator. The multiple load approach is done by varying the impedance at the downstream end. For $M = 0.025$ and $M = 0.100$ only a multiple source approach is done. These flow rates are at the lower limit of the operating range of one roots blower or the parallel roots blower configuration. For this reason, it is not possible to keep the flow rate constant when the muffler at the downstream end is removed to achieve a multiple load condition.

A LMS Scadas III multichannel data acquisition system is used, in combination with LMS Test.Lab Rev.13A for the first data processing. All experiments are carried out with a stepped sine excitation, from 20 Hz to 1700 Hz, with a frequency step of 10 Hz. The number of averages is chosen depending on the expected signal-to-noise ratio, with an increased number of averages per measurement for the flow rates where only two measurements could be carried out. Before further processing the data, all microphone signals with a low coherence with respect to the excitation signal are discarded. The processing of the data is carried out with the iterative procedure of reference[46] . The procedure runs for 300 iterations or until convergence of the results. Table 1 gives an overview of the different measurement and processing parameters for all flow rates.

**Table 1. Measurement and processing parameters**

| target $M$ | # averages | # measurements | coherence threshold |
|---|---|---|---|
| 0 | 300 | 2 | 0.9 |
| 0.025 | 1000 | 2 | 0.9 |
| 0.05 | 600 | 4 | 0.9 |
| 0.075 | 600 | 4 | 0.9 |
| 0.1 | 1000 | 2 | 0.9 |



## C. Numerical setup

The numerical techniques described in section 4 are applied to the slit resonator geometry. To limit the required computational power, only two-dimensional simulations have been carried out. Figure 5 shows the computational domain used in the simulations, which is a cross section of the 2,5D geometry of the test section used in the experiments.

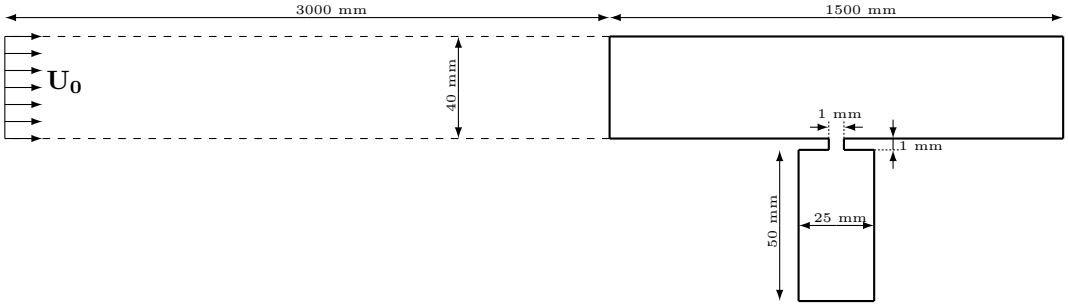


**Figure 5. Schematic overview of the geometry under consideration (not to scale!). The thick lines indicate the computational domain used for the acoustic simulations with the LNSE, the thin lines show the extended domain used for the mean flow simulations.**

The use of the LNSE requires the mean flow field to be known. Therefore a two-step approach is used, where first the mean flow field is computed using a steady CFD simulation and in a second step, the acoustic field and its interaction with the mean flow is solved using the LNSE.

### *1. Mean flow simulation*

The mean flow field is computed using a steady RANS simulation, carried out with the commercial CFD software ANSYS Fluent. The k-$\omega$ SST model is solved all the way down to the walls ($y^+ < 1$) using the

SIMPLE algorithm, no specific wall modelling is used. The spatial discretization is a standard finite volume method, where the convective terms are discretized with second-order upwind fluxes and central fluxes are used for the viscous terms.

Seen the long pipe length before the test section in the experiments, it is assumed that the flow in the duct is fully developed. In order to obtain a fully developed flow at the inlet of the computational domain used for the LNSE simulations, the channel has been extended 3 m upstream and a uniform velocity is imposed at the inlet. Figure 6 shows the axial velocity profile for an inlet Mach number of $M = 0.075$ at the inlet of the acoustic domain, and 250 mm and 500 mm upstream of this plane, confirming that the mean flow is fully developed when it enters the computational domain of the acoustic simulations. In the following sections, the indicated Mach numbers refer to the imposed uniform inlet velocity.

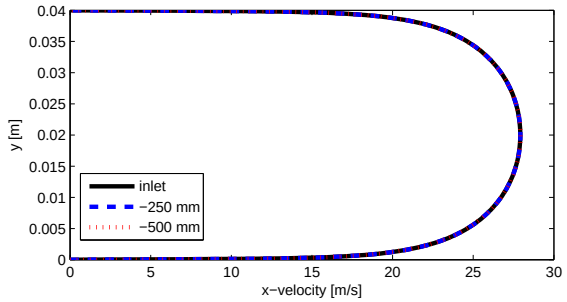


**Figure 6. X-velocity at the inlet of the acoustic domain (-) and 250 mm (- -) and 500 mm (• • •) before the inlet of the acoustic domain for an inlet Mach number of $M = 0.075$.**

Figure 7 shows the velocity field near the perforation for an inlet Mach number of $M = 0.075$. As expected, the flow is mainly grazing over the facing sheet, with only a weak clockwise circulation inside the orifice. The air in the cavity is nearly quiescent. For the other Mach numbers considered in this paper, a similar mean flow field is obtained.



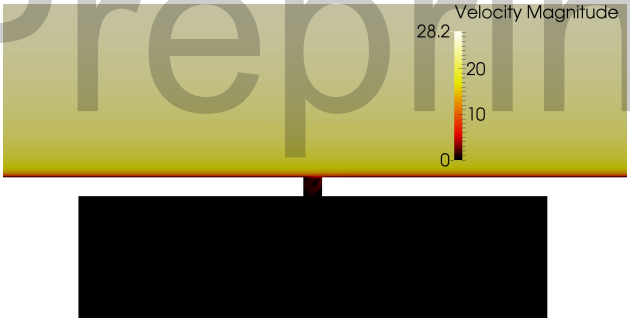


**Figure 7. Mean flow velocity magnitude near the orifice for an inlet Mach number of $M = 0.075$.**

The solution of the RANS simulation has to be mapped from the fine CFD grid to the coarser acoustic grid. For the RKDG method, this is done using the local least-squares interpolation procedure of reference[22] . The pFEM method uses linear fitting for both field variables and derivatives or polynomial least-squares interpolation fitting for the CFD data mapping. In the present configuration, first approach has been found to be sufficient and it requires less computational time. The same RANS solution is used as input for both LNSE methods.

### *2. Acoustic simulation*

The RKDG and pFEM simulations of the acoustic field have been performed on a 2-D computational mesh with 1505 triangular elements (figure 8) and $4^{\text{th}}$-order interpolating polynomial functions. Although this mesh is not fine enough to resolve the acoustic boundary layer, it is sufficient to model the phenomena governing the interaction between the grazing flow and the acoustics of this case.

In the frequency domain pFEM method, simulations have been carried out for 50 frequencies, equally spaced in the given frequency range, with a frequency step of 36 Hz. In time domain, a pulse excitation is applied at the in- or outlet of the duct and the simulation runs until all energy has left the system. The

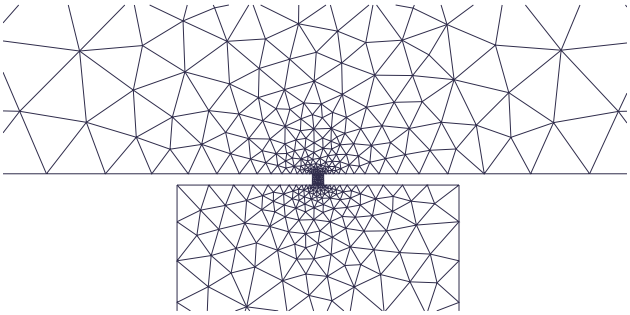

**Figure 8. Close-up of the mesh used for the frequency domain pFEM and time-domain RKDG acoustic simulations .**

results are transformed to the frequency-domain using an FFT-algorithm before further processing. The frequency resolution, determined by the total simulated time, is approximately 15.5 Hz. The kinematic viscosity of air is set to $\nu = 1.46e^{-5}\, m^2/s$.

The pressure fluctuations are stored at the points required for the different impedance measurement techniques described in section III. For the in-situ impedance measurement method, the pressure fluctuations at the facing sheet and at the bottom of the cavity are required. In order to average out the influence of the hydrodynamic component of the pressure, the facing sheet pressure is recorded at 9 points on a half circle with radius $d/2$ around the orifice and the signals are averaged before further processing. At the bottom of the cavity, the pressure is averaged over 3 points against the bottom wall.

The impedance eduction methods are based on the determination of the scatter matrix of a duct segment around the orifice. This duct segment corresponds to the part of the duct above the cavity and therefore has a length of 25 mm. The scatter matrix is computed with the technique described in section III, requiring the pressure fluctuations in at least two points in the in- and outlet duct. Like in the experimental two-port characterization, 4 measurement positions are used in each duct in order to cover the full frequency range of interest. These planes are located at a distance $z_i = \pm 0.08$m, $\pm 0.15$m, $\pm 0.27$m and $\pm 0.50$m from the center of the perforation. At each of these positions, the pressure is recorded at 8 equally spaced points across the cross section of the channel. The averaged pressure fluctuations at each cross section are used in equation (10) instead of the pressure at one specific point in order to suppress the influence of the decaying cut-off modes.



## IV. Discussion of the results

### A. Comparison of the numerical techniques

Figure 9 shows the absolute value of the scatter matrix components for different flow velocities obtained from the RKDG simulations and the pFEM simulations. Some discrepancies can be observed between the RKDG and the pFEM results, especially at low grazing flow velocities. The RKDG results have a lower resonance frequency and show a more damped behavior than the pFEM results. Since the mesh, the parameters and the post-processing are identical for both methods, the discrepancies have to be related to inherent differences between the RKDG and the pFEM method and implementation. The main cause is probably the treatment of the viscous terms, which is completely different for both methods: the RKDG method uses a two-step approach, first computing the velocity gradients as independent variables while the pFEM formulation solves the LNSE in one step.

This hypothesis is supported by figure 10, showing the absolute value of the scatter matrix components for a resonator with a slit of 2 mm wide in a quiescent medium. All other parameters are identical to the present case. For this resonator, the discrepancies between the pFEM and RKDG results are significantly smaller. Since only the size of the orifice has been changed with respect to figure 9, the discrepancies are caused by phenomena localized around the orifice. The importance of the viscous effects is determined by the velocity gradients, which are strongest around the orifice. Increasing the orifice width decreases the velocity gradients and hence the influence of the viscosity. Because in this case also the discrepancies between the RKDG and the pFEM results reduce significantly, it is likely that they are caused by the treatment of the viscous terms.

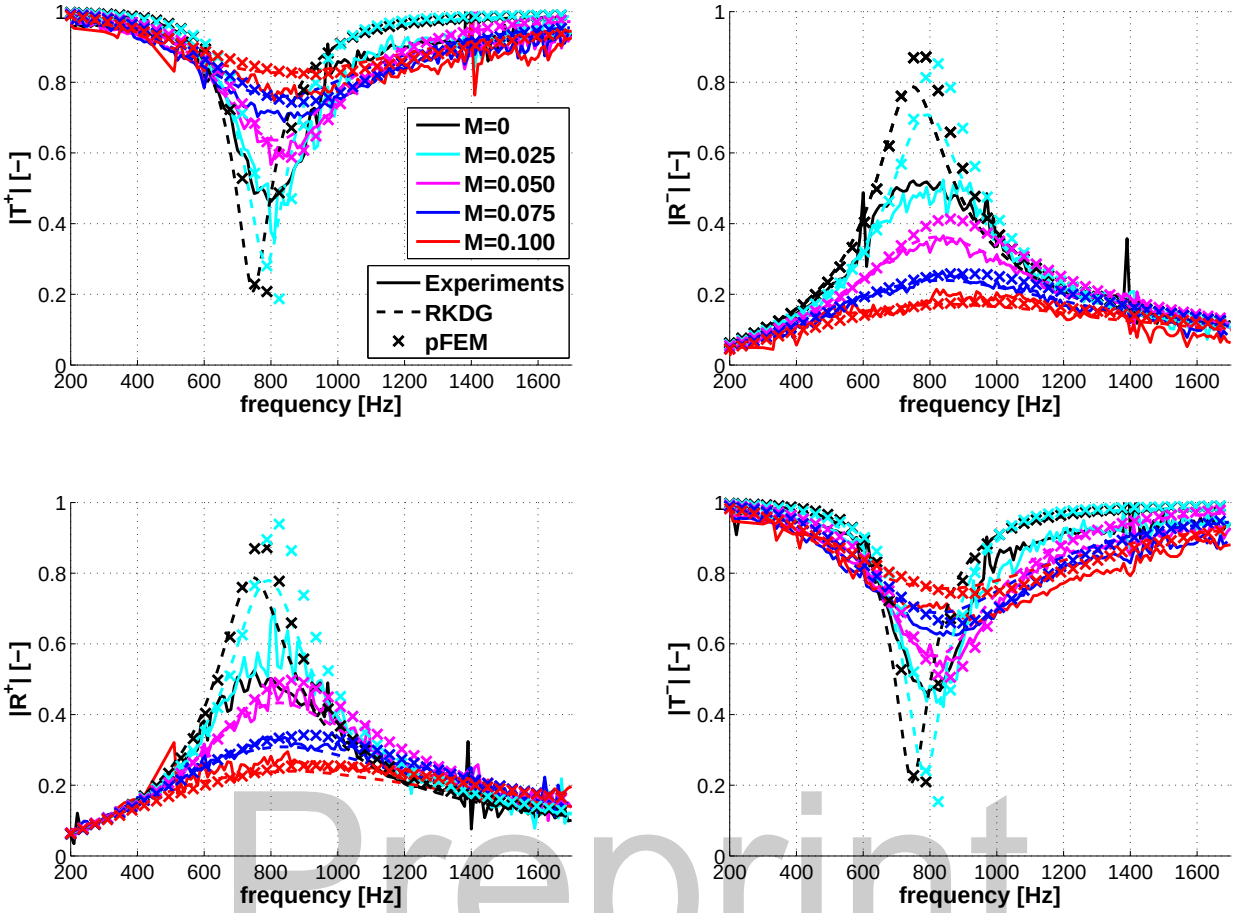




**Figure 9. Absolute value of the scatter matrix coefficients for different mean flow Mach numbers, $M = 0$ (black), $M = 0.025$ (cyan), $M = 0.05$ (magenta), $M = 0.075$ (blue), $M = 0.1$ (red): comparison between simulation results of the RKDG ($--$) and pFEM ($\times$) methods and experiments ($-$).**

Figure 9 shows that the differences between the two methods decrease for higher grazing flow velocities. This also supports the hypothesis that the differences are related to the viscous terms. Indeed, at higher flow velocities, the losses related to the interaction of the acoustic field with the shear layer over the orifice will dominate the viscous scrubbing losses in and around the orifice.

## B. Comparison with experiments

Figure 9 also shows the scatter matrix components determined experimentally. At low flow velocities, the experimental results show a much more damped behavior than the numerical results. This was expected, since the viscous scrubbing losses dominate the damping in the system at these flow velocities and the acoustic boundary layer was not resolved in the simulations. Therefore, the viscous losses are underestimated by the simulations, resulting in less damped behavior of the scatter matrix coefficients.

At higher flow rates, the interaction with the shear layer becomes the dominant mechanism. Since the LNSE are capable of simulating the linear interaction between the acoustic field and the mean flow, the simulated coefficients are much closer to the experimental curves at higher flow velocities. Also, although significant differences between simulations and experiments are observed, it is clear that the correct trend with increasing flow velocity is obtained.

Different factors can explain the differences between the simulations and the experiments, amongst others:

- It was assumed that the flow is fully developed when it enters the acoustic domain. This was however not verified experimentally. Also other factors influencing the mean flow profile, such as turbulence

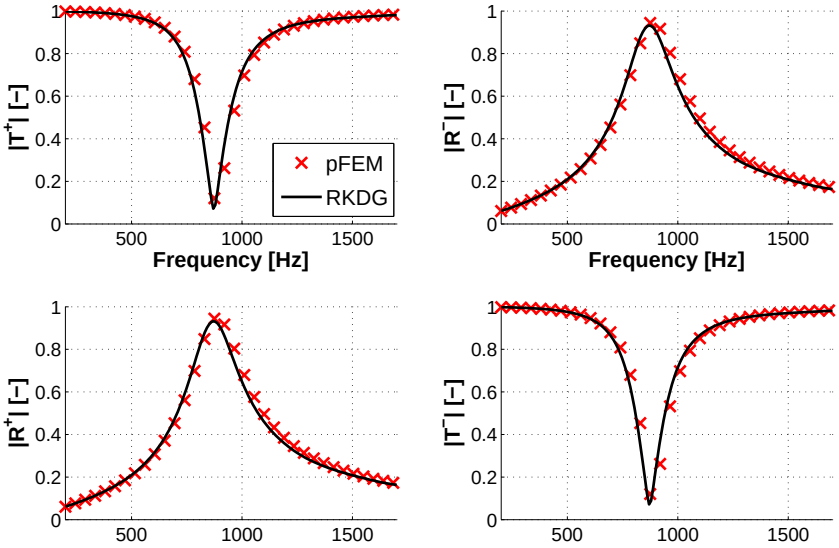


**Figure 10. Absolute value of the scatter matrix coefficients, computed with the RKDG (–) and pFEM (×) method, for a resonator with a slit of 2 mm wide in a quiescent medium. All other dimensions identical to the resonator of figure 5.**

levels, have not been verified. It is therefore likely that the simulated mean flow does not correspond exactly to the experimental situation.

- The simulations were carried out on a 2,5D slit resonator geometry in a rectangular duct, while the simulations considered a 2D geometry. Although a high aspect ratio was used in the experiments, 3D effects can not be excluded.

Taking these factors into account, the agreement is deemed satisfactory.



### C. Comparison of the impedance measurement techniques

Figure 11 shows the impedance of the resonator, computed from the simulation results with the three methods described in section III. Because of the assumptions of the models used in the impedance eduction techniques, the lumped approach can only provide the impedance at low frequencies and the distributed approach is only valid at high frequencies. For this reason, the curves corresponding to these methods have been arbitrarily limited to 200 Hz - 850 Hz ($kw \leq 0.4$) for the lumped approach and 650 Hz - 1700 Hz ($kw \geq 0.3$) for the distributed approach. The in-situ method is valid over the full frequency range of interest (200 - 1700 Hz).

The same conclusions with respect to the differences between the pFEM and the RKDG results as in section A apply. Consistently with the hypothesis that the cause of the discrepancies is the treatment of the viscous terms, the largest scatter is seen for the resistance results. For the reactance, good agreement between the results of the RKDG and the pFEM simulations is obtained for all impedance measurement techniques, especially at low frequencies. The pFEM simulations however predict a slightly lower reactance over the full frequency range and for all flow velocities.

Comparing the different measurement techniques, no clear trends can be observed regarding the resistance. Furthermore, it was noticed that obtaining the resistance with the in-situ method is a challenging task. A small variation of the measurement position at the facing sheet can result in a completely different resistance curve. This once more confirms the uncertainty regarding the viscous effects in and around the orifice.

The reactance curves obtained with the in-situ technique are much less sensitive with respect to the facing sheet measurement position and the results of the different techniques show some clear trends. The reactance obtained with the lumped approach is systematically higher than the one obtained with the in-situ technique. However, the lumped approach is based on the assumption of local incompressibility. The poor agreement with the other techniques suggests that this assumption is no longer valid in the frequency range of interest.

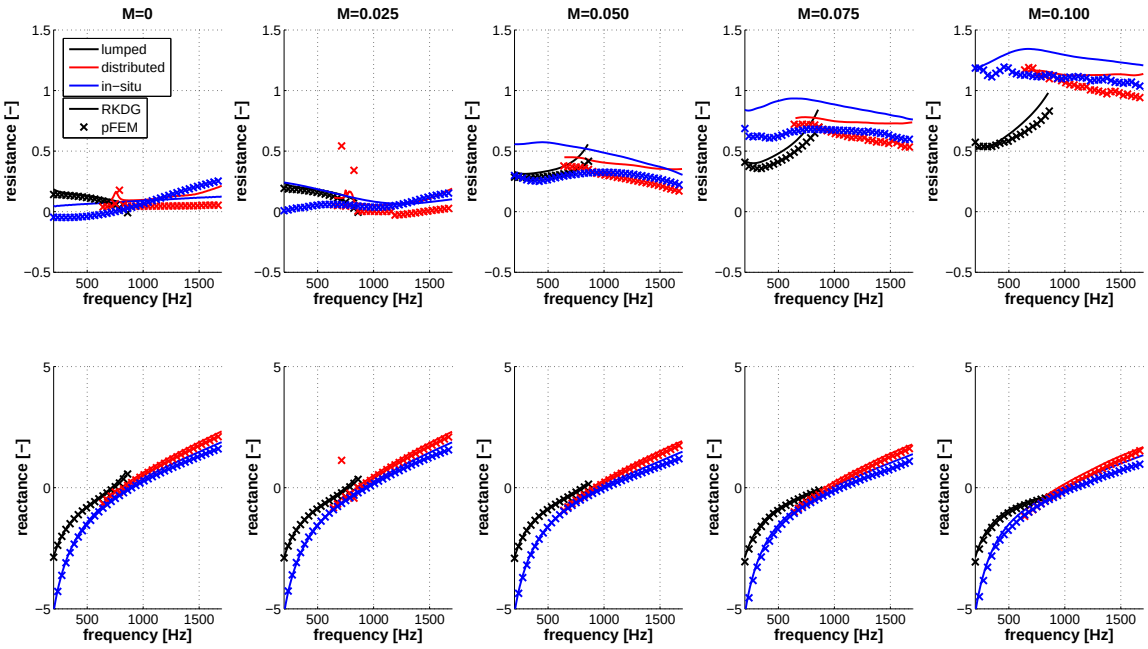


**Figure 11. Resistance (top) and reactance (bottom), obtained with the in-situ method (blue), the lumped impedance eduction (black) and the distributed impedance eduction approach (red) from the simulation results of the RKDG code (−) and the pFEM code (×).**



The in-situ technique and the distributed impedance eduction show a reasonable agreement at the lower frequencies, but the agreement deteriorates with increasing frequency. The reactance given by the in-situ technique is systematically lower than the one obtained from the distributed impedance eduction technique. Since the in-situ technique relies on pressure data around the orifice, it is expected that the results of the impedance eduction technique are more reliable.

Although there is significant scatter between the impedance obtained experimentally and numerically with the different methods, they all show the same behavior of the impedance as a function of grazing flow velocity. Figure 12 shows the impedance, educed with the lumped and the distributed approach for different grazing flow velocities. At low grazing flow velocities (up to $M = 0.025$), for both simulation results and experimental data, the difference with the case of a quiescent medium is small and no clear trend can be observed. However, for higher flow velocities ($M = 0.050$ and higher), the resistance significantly increases with increasing Mach number and the reactance slightly decreases, shifting the resonance frequency to higher frequencies. These observations are in agreement with earlier experimental[9–14] and numerical[6,21] observations on Helmholtz resonators with various geometries.

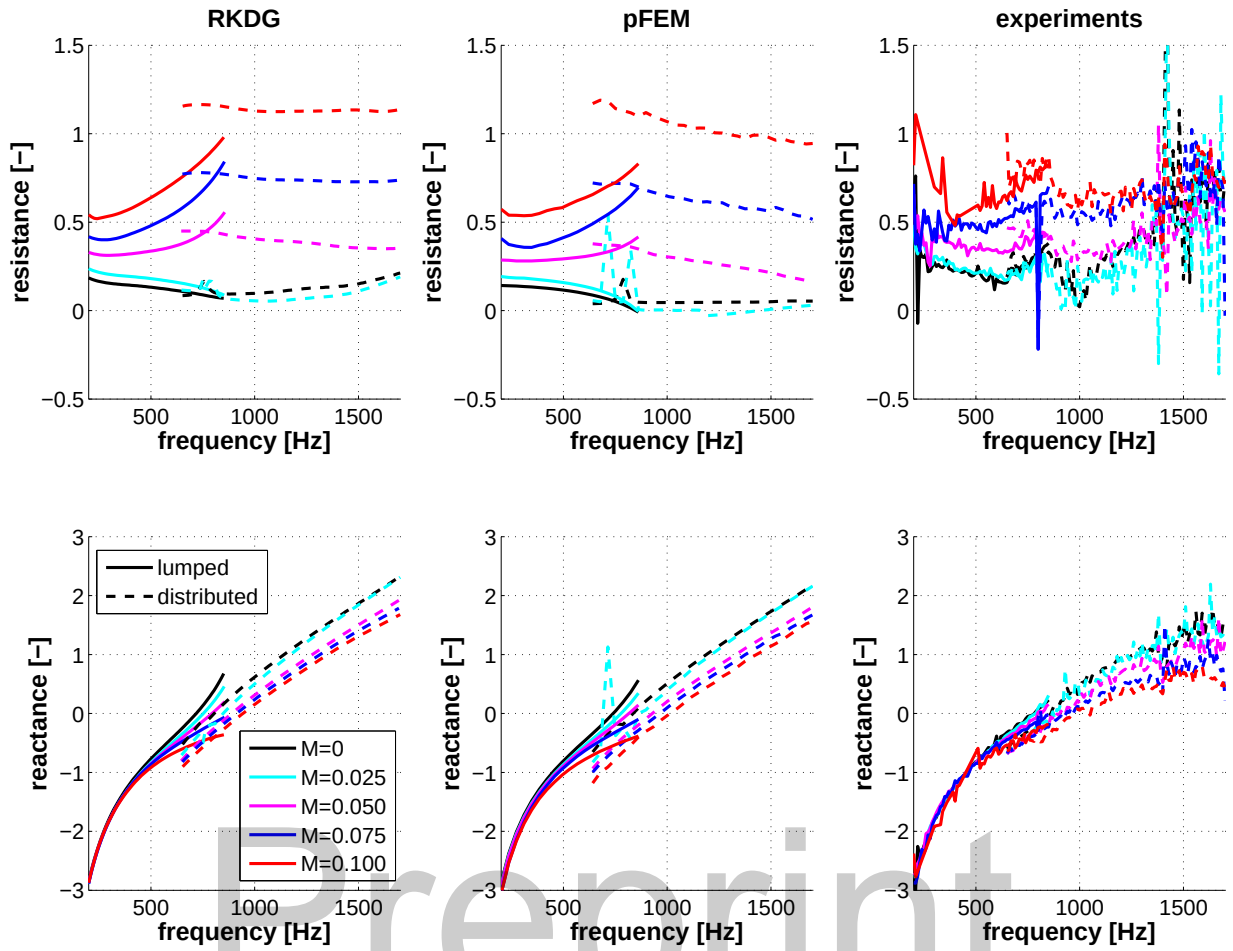


**Figure 12. Resistance (top) and reactance (bottom), obtained with the lumped impedance eduction (–) and the distributed impedance eduction (– –) from the RKDG simulations (left), the pFEM simulations (middle) and the experiments (right) for different grazing flow velocities.**



## V. Conclusion

The goal of this study is to compare two numerical methods implementing the linearized Navier-Stokes equations for the acoustic characterization of a slit resonator under grazing flow: a frequency domain high-order finite element method and a time-domain Runge-Kutta discontinuous Galerkin method. The simulations showed a reasonable agreement, although some remarkable discrepancies were observed. The analysis seems to indicate that the discrepancies are related to the different treatment of the viscous terms of the LNSE in the two implementations.

The simulation results were compared to experimental data, obtained from a dedicated measurement campaign on a slit resonator. It was shown that the simulations predict the correct trends with respect to the grazing flow velocity.

Different impedance measurement techniques were applied to the simulation results. Significant differences between the different techniques could be observed. Especially for the resistance, a large scatter on the results is observed. This can be explained by the discrepancies between the simulation results caused by the treatment of viscosity. The different impedance measurement techniques show reasonable agreement for the reactance, although some systematic differences can be observed. All impedance measurement techniques predict the same trends with respect to the grazing flow velocity, which is confirmed by the experimental results.

## Acknowledgments

The research of Hervé Denayer is funded by a fellowship of the Agency for Innovation by Science and Technology in Flanders (IWT). The presented work is part of the Marie Curie Initial Training Network Thermo-acoustic and aero-acoustic nonlinearities in green combustors with orifice structures (TANGO). We gratefully acknowledge the financial support from the European Commission under call FP7-PEOPLE-ITN-2012.

## References

[1]C. K. W. Tam and K. A. Kurbatskii, "Microfluid dynamics and acoustics of resonant liners," *AIAA Journal*, vol. 38, pp. 1331–1339, 2000.

[2]C. K. W. Tam, K. A. Kurbatskii, K. K. Ahuja, and J. R. J. Gaeta, "A numerical and experimental investigation of the dissipation mechanisms of resonant acoustic liners," *Journal of Sound and Vibration*, vol. 245, pp. 545–557, 2001.

[3]C. K. W. Tam, H. Ju, M. G. Jones, W. R. Watson, and T. L. Parrott, "A computational and experimental study of slit resonators," *Journal of Sound and Vibration*, vol. 284, pp. 947–984, 2005.

[4]C. K. Tam, H. Ju, and B. E. Walker, "Numerical simulation of a slit resonator in a grazing flow under acoustic excitation," *Journal of Sound and Vibration*, vol. 313, pp. 449–471, 2008.

[5]C. K. W. Tam, H. Ju, M. G. Jones, W. R. Watson, and T. L. Parrott, "A computational and experimental study of resonators in three dimensions," in *Proceedings of the 15th AIAA/CEAS Aeroacoustics Conference*, no. AIAA 2009-3171, 2009.

[6]Q. Zhang and D. J. Bodony, "Numerical simulation of two-dimensional acoustic liners with high-speed grazing flow," *AIAA Journal*, vol. 49, no. 2, pp. 365–382, 2011.

[7]Q. Zhang and D. J. Bodony, "Impedance predictions of 3D honeycomb liner with circular apertures by DNS," in *Proceedings of the 17th AIAA/CEAS Aeroacoustics Conference*, no. AIAA 2011-2727, 2011.

[8]Q. Zhang and D. J. Bodony, "Numerical investigation and modelling of acoustically excited flow through a circular orifice backed by a hexagonal cavity," *Journal of Fluid Mechanics*, vol. 693, pp. 367–401, 2012.

[9]A. S. Hersh and B. Walker, "Effect of grazing flow on the acoustic impedance of helmholtz resonators consisting of single and clustered orifices," Tech. Rep. NASA CR-3177, NASA, 1979.

[10]J. W. Kooi and S. L. Sarin, "An experimental study of the acoustic impedance of helmholtz resonator arrays under a turbulent boundary layer," in *AIAA 7th Aeroacoustics Conference*, no. AIAA-81-1998, 1981.

[11]B. E. Walker and A. F. Charwat, "Correlation of the effects of grazing flow on the impedance of helmholtz resonators," *Journal of the Acoustical Society of America*, vol. 72, pp. 550–555, 1982.

[12]A. Cummings, "The effects of grazing turbulent pipe-flow on the impedance of an orifice," *Acustica*, vol. 61, pp. 233–242, 1986.

[13]G. Ajello, *Mesures acoustiques dans les guides d'ondes en présence d'écoulement: Mise au point d'un banc de mesure: Applications à des discontinuités*. PhD thesis, Université du Maine, 1997.

[14]X. Jing, X. Sun, J. Wu, and K. Meng, "Effect of grazing flow on the acoustic impedance of an orifice," *AIAA Journal*, vol. 39, no. 8, pp. 1478–1483, 2001.

[15]I. D. J. Dupère and A. P. Dowling, "The absorption of sound by helmholtz resonators with and without flow," in *Proceedings of the 8th AIAA/CEAS Aeroacoustics Conference & Exhibit*, no. AIAA 2002-2590, 2002.

[16]S. K. Tang, "On sound transmission loss across a helmholtz resonator in a low mach number flow duct," *The Journal of the Acoustical Society of America*, vol. 127, no. 6, pp. 3519–3525, 2010.

[17]A. Kierkegaard, S. Boij, and G. Efraimsson, "A frequency domain linearized navier-stokes equations approach to acoustic propagation in flow ducts with sharp edges," *Journal of the Acoustical Society of America*, vol. 127, pp. 710–719, 2010.

[18]A. Kierkegaard, S. Boij, and G. Efraimsson, "Simulations of the scattering of sound waves at a sudden area expansion," *Journal of Sound and Vibration*, vol. 331, pp. 1068–1083, 2012.

[19]A. Kierkegaard, S. Allam, G. Efraimsson, and M. Åbom, "Simulations of whistling and the whistling potentiality of an in-duct orifice with linear aeroacoustics," *Journal of Sound and Vibration*, vol. 331, pp. 1084–1096, 2012.

[20]A. Kierkegaard, G. Efraimsson, and A. Agarwal, "Linear simulations of liners sandwiched with a metal foam," in *Proceedings of the 19th AIAA/CEAS Aeroacoustics Conference*, no. AIAA 2013-2272, American Institute of Aeronautics and Astronautics, May 2013.

[21]H. Denayer, W. De Roeck, W. Desmet, and T. Toulorge, "Acoustic characterization of a helmholtz resonator under grazing flow conditions using a hybrid methodology," in *Proceedings of the 19th AIAA/CEAS Aeroacoustics Conference*, no. AIAA 2013-2076, 2013.

[22]T. Toulorge, *Efficient Runge-Kutta Discontinuous Galerkin Methods Applied to Aeroacoustics*. PhD thesis, KU Leuven, 2012.

[23]T. Toulorge, W. De Roeck, H. Denayer, and W. Desmet, "Computational aeroacoustic characterization of different orrifice geometries under grazing flow conditions," in *Proceedings of the International Conference on Noise and Vibration Engineering ISMA 2012* (P. Sas, D. Moens, and S. Jonckheere, eds.), (Leuven, Belgium), pp. 617–631, September 17–19 2012.

[24]S. Boij and B. Nilsson, "Reflection of sound at area expansions in a flow duct," *Journal of sound and vibration*, vol. 260, pp. 477–498, 2003.

[25]G. Gabard, "Discontinuous galerkin methods with plane waves for time-harmonic problems," *Journal of Computational Physics*, vol. 225, no. 2, pp. 1961–1984, 2007.

[26]R. Ewert and W. Schroeder, "Acoustic perturbation equations based on flow decomposition via source filtering," *Journal of computational physics*, vol. 188, pp. 365–398, 2003.

[27]P. Solin, K. Segeth, and I. Dolezel, *Higher-Order Finite Element Methods*. 2004.

[28]O. Zienkiewicz, R. Taylor, and P. Nithiarasu, *The finite element method for fluid Dynamics*. Elsevier, 2005.

[29]G. Gabard, "Formulation of the wave-based discontinuous galerkin methods." December 2012.

[30]H. Bériot, G. Gabard, and E. Perrey-Debain, "Analysis of high-order finite elements for convected wave propagation," *International journal for numerical methods in engineering*, 2013.

[31]J. Connor and C. Brebbia, *Finite element technique for fluid flow*. Newnes-Butterworhths, 1976.

[32]W. De Roeck, *Hybrid methodologies for the computational aeroacoustic analysis of confined, subsonic flows*. PhD thesis, K.U. Leuven, 2007.

[33]F. Bassi and S. Rebay, "A high-order accurate Discontinuous finite element method for the numerical solution of the compressible Navier-Stokes equations," *Journal of Computational Physics*, vol. 131, no. 2, pp. 267–279, 1997.

[34]D. N. Arnold, F. Brezzi, B. Cockburn, and L. D. Marini, "Unified analysis of discontinuous galerkin methods for elliptic problems," *SIAM Journal on Numerical Analysis*, vol. 39, no. 5, pp. 1749–1779, 2002.

[35]F. Bassi, A. Crivellini, S. Rebay, and M. Savini, "Discontinuous Galerkin solution of the Reynolds-averaged Navier-Stokes and $k$-$\omega$ turbulence model equations," *Computers & Fluids*, vol. 34, pp. 507–540, 2005.

[36]T. Suzuki and S. K. Lele, "Green's functions in a boundary layer: low and high frequency asymptotes," in *6th AIAA/CEAS Aeroacoustics Conference & Exhibit*, no. AIAA 2000-2071, 2000.

[37]T. Suzuki and S. Lele, "Green's functions for a source in a boundary layer: direct waves, chanelled waves and diffracted waves," *J. Fluid Mech.*, vol. 477, pp. 129–173, 2003.

[38]M. Bauer, J. Dierke, and R. Erwert, "Application of a discontinuous galerkin method to predict airframe noise," *Proceedings of the 15th AIAA/CEAS Aeroacoustics Conference*, May 2009.

[39]K. Ehrenfield, C. Meyer, and A. Dillmann, "Simulation of sound propagation in boundary layers based on moehring's acoustic analogy," in *9th AIAA/CEAS Aeroacoustics Conference and Exhibit*, no. AIAA 2003-3272, 2003.

[40]P. D. Dean, "An in situ method of wall acoustic impedance measurement in flow ducts," *Journal of Sound and Vibration*, vol. 34, pp. 97–130, 1974.

[41]W. Schuster, "A comparison of ensemble averaging methods using dean's method for in-situ impedance measurements," in *Proceedings of the 18th AIAA/CEAS Aeroacoustics Conference*, no. AIAA 2012-2244, Jun 2012.

[42]Q. Zhang and D. J. Bodony, "Impedance prediction of three-dimensional honeycomb liners with laminar/turbulent boundary layers using dns," in *Proceedings of the 19th AIAA/CEAS Aeroacoustics Conference*, no. AIAA 2013-2268, May 2013.

[43]M. Åbom, "Measurement of the scattering-matrix of acoustical two-ports," *Mechanical Systems and Signal Processing*, vol. 5, no. 2, pp. 89–104, 1991.

[44]S.-H. Jang and J.-G. Ih, "On the multiple microphone method for measuring in-duct acoustic properties in the presence of mean flow," *Journal of the Acoustical Society of America*, vol. 103, no. 3, pp. 1520–1526, 1998.

[45]W. De Roeck, L. Nordström, T. Englund, and W. Desmet, "Experimental two-port characterization of the aeroacoustic transmission properties of a truck's exhaust system," *SAE International Journal of Passenger Cars - Mechanical Systems*, vol. 5, Jun 2012.

[46]H. Denayer, W. De Roeck, and W. Desmet, "Optimized plane-wave decomposition for accurate two-port characterization," in *Proceedings of the International Conference on Noise and Vibration Engineering ISMA 2014* (P. Sas, D. Moens, and H. Denayer, eds.), (Leuven, Belgium), September 15–17 2014.

[47]M. Munjal, *Acoustics of ducts and mufflers with application to exhaust and ventilation system design*. John Wiley & Sons, 1987.

[48]L. D. Santana, W. De Roeck, W. Desmet, and P. Ferrante, "Two-port indirect acoustic impedance eduction in presence of grazing flows," in *Proceedings of the 17th AIAA/CEAS Aeroacoustics Conference*, no. AIAA 2011-2868, 2011.

[49]W. De Roeck and W. Desmet, "Experimental analysis of the aerodynamic noise generating mechanisms in a simple expansion chamber," in *Proceedings of the 14th AIAA/CEAS Aeroacoustics Conference*, no. AIAA 2008-3055, 2008.

[50]W. De Roeck and W. Desmet, "Experimental acoustic identification of flow noise sources in expansion chambers," in *Proceedings of ISMA 2008*, pp. 455–470, 2008.